



Facile scalable synthesis of graphene oxide and reduced graphene oxide: comparative investigation of different reduction methods

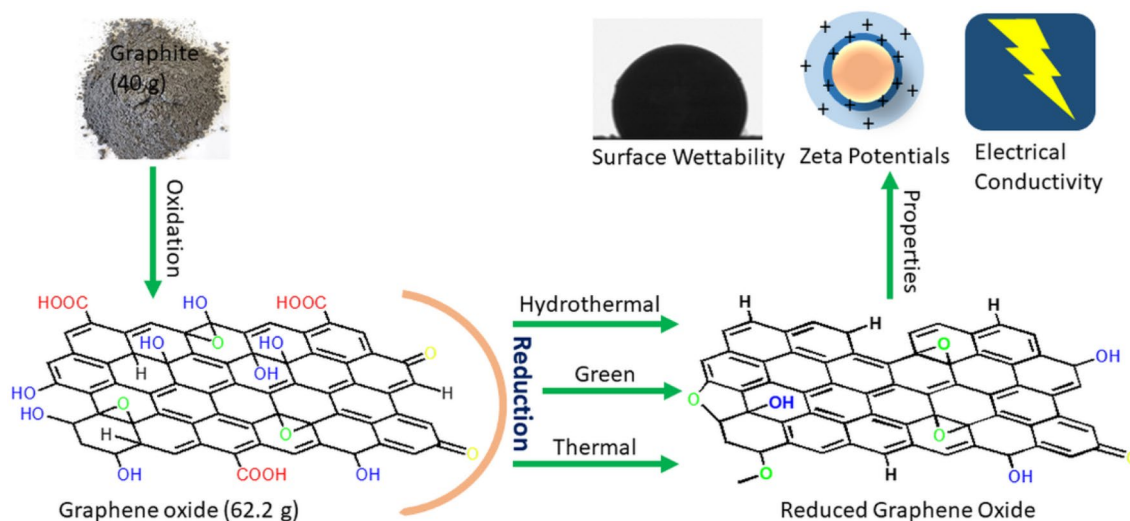
Neeraj Kumar^{1,2} · Katlego Setshedi¹ · Mike Masukume¹ · Suprakas Sinha Ray^{1,2}

Received: 8 December 2021 / Revised: 25 February 2022 / Accepted: 7 March 2022 / Published online: 28 March 2022
© The Author(s), under exclusive licence to Korean Carbon Society 2022

Abstract

As frontier materials, graphene oxide (GO) and graphene have penetrated almost all research areas and advanced numerous technologies in sensing, electronics, energy storage, catalysis, water treatment, advanced composites, biomedical, and more. However, the affordable large-scale synthesis of high-quality GO and graphene remains a significant challenge that negatively affects its commercialisation. In this article, firstly, a simple, scalable approach was demonstrated to synthesise high-quality, high yield GO by modifying the improved Hummers method. The advantages of the optimised process are reduced oxidation time, straightforward washing steps without using coagulation step, reduction in cost as eliminating the use of phosphoric acid, use of minimum chemical reagents, and increased production of GO per batch (~62 g). Subsequently, the produced GO was reduced to reduced graphene oxide (rGO) using three different approaches: green reduction using ascorbic acid, hydrothermal and thermal reduction techniques. The GO and rGO samples were characterised using various microscopy and spectroscopy techniques such as XRD, Raman, SEM, TEM, XPS and TGA. The rGO prepared using different methods were compared thoroughly, and it was noticed that rGO produced by ascorbic acid reduction has high quality and high yield. Furthermore, surface (surface wettability, zeta potential and surface area) and electrical properties of GO and different rGO were evaluated. The presented synthesis processes might be potentially scaled up for large-scale production of GO and rGO.

Graphical abstract



Keywords Graphite oxidation · Scalable production · Graphene oxide reduction · Graphene properties · Electrical characteristics

1 Introduction

By virtue of flat structure and extraordinary properties, graphene materials have entered almost every arena of research from energy production and storage [1, 2], electronics [3], catalysis [4], composites [5], environmental remediation [6–8] to biomedical [9]. For example, graphene has shown widespread uses in better performing electrode materials. It enables the fabrication of highly efficient energy storage devices (Li-ion/metal-air batteries, fuel cells, and supercapacitors) [10, 11], solar fuel production devices [12], electro-catalytic devices for water/air purification [13, 14] and value-added chemical production [15, 16]. Bulk and commercially viable graphene materials will be needed to realise the above applications at a large scale. Moreover, most of the “commercial graphene” in the market for customers is not graphene but rather expensive graphite that has posed serious worries from customers and the booming million-dollar graphene industry [17–19]. Thus, improving existing synthesis methods and developing new scalable methods for low-cost, large-scale production of best-quality graphene materials are highly crucial.

Various bottom-up (chemical vapour deposition or epitaxial growth) and top-down (mechanical exfoliation, liquid-phase exfoliation, chemical exfoliation using strong oxidants) methods have been developed to synthesise graphene [20]. For the commercial applications of graphene, the production route should assure good quality, few-layer distribution, affordable cost, and reproducible high yield eco-friendly process. The chemical vapour deposition or epitaxial growth provides a large area (up to 7.5 m²) of high-quality graphene that is useful for high-end applications (viz. advanced electronics) [21–24]. Besides recent improvements to reduce the cost, these processes are still expensive due to multistep reactions, require metal catalysts and complicated instruments and lack of mass production protocols [20, 23]. The mechanical exfoliation method offers the best quality of graphene, but the process is tedious, cannot be scaled up [25]. Liquid-phase exfoliation of graphite primarily produces lower-grade (graphene nanoplatelets) with low yield [20]. Contrarily, the solution-processed chemical exfoliation approach is desirable for mass-scale production with comparatively lower costs and tailorable graphene. It produces graphene with oxygen-carrying functional groups on the edge sites and basal plane, which are helpful to fabricate advanced functional materials [23, 26, 27].

In the chemical oxidative-exfoliation, graphite (cheap and abundantly available source) is first oxidised to graphite oxide before exfoliating to few-layer graphene oxide (GO). The GO may then undergo reduction either

chemically/hydrothermally or thermally to eliminate oxygen-carrying functionalities to yield reduced graphene oxide (rGO). Numerous synthetic protocols for GO preparation have been developed that vary the potent oxidising reagent, the co-oxidising agent, the strong acid intercalant, and the relative amounts of each precursor [20, 28]. The synthetic routes have improved over time to employ more practical protocols, materials, and process safety. Among previously developed oxidation protocols (Brodie [29], Staudenmaier [30], and Hummers and Offeman [31]), Hummers’ method is mainly used for GO synthesis as it requires a short reaction time and is comparatively less hazardous. However, the release of toxic gases, low yield and residual nitrate content are drawbacks of Hummer’s process.

Furthermore, several modifications have been proposed in Hummer’s method to obtain GO with a high yield and high degree of oxidation. Marcano et al. showed improvements in the degree of oxidation by replacing NaNO₃ with H₃PO₄ in Hummers’ chemicals (KMnO₄, H₂SO₄, and NaNO₃) [27]. They claimed that the proposed method did not release toxic gases and could produce a higher yield of hydrophilic GO with some impurities of cyclic phosphate groups. However, the elimination of phosphate impurities is not addressed, and separation/purification processes are tedious in this process. They have demonstrated the oxidation of few grams (3 g) of graphite only. Peng et al. [32] developed a potassium ferrate-based procedure for oxidation of graphite to GO by replacing KMnO₄ and NaNO₃ from Hummers’ method. However, the used oxidant (potassium ferrate) is expensive, and this method also presented oxidation of a low quantity of graphite (10 g). Chen et al. [33] demonstrated the process that eliminates the uses for NaNO₃ to form graphite oxide (less amount) and illustrated the simplified approach to purify waste solution after the reaction. Although this method eliminates the release of toxic NO_x gases, but it is not scalable because it needs a high temperature for operation (95 °C) and requires exothermic addition of water in an acid mixture.

To date, the synthesis of GO using Hummers’ and its modified versions have been widely explored at a laboratory scale, but limited efforts have been made for the demonstration of a scalable approach [34, 35]. The produced amount in these synthesis routes is significantly less (few grams), which is not sufficient for the processing of GO for the composite application; for example, graphene-based polymer composite processing requires more than 10 g of GO/rGO in a single batch. Using two different batches might create chances of errors and inconsistency in results. Thus, developing a low-cost scalable route for high-grade GO production using minimum chemical reagents and environmental footprints is of utmost importance. The objective of this study is to develop affordable routes for GO and rGO

production. Herein, a simple, scalable GO production route without using NaNO_3 and H_3PO_4 has been developed that yield ~62 g of GO in a single batch. The optimal conditions were identified to reduce the quantities of chemical reagents and reaction time used during the synthesis. The produced GO was further then reduced to rGO using three different scalable reduction methods, namely hydrothermal reduction (H-rGO), green reduction using ascorbic acid (AA-rGO) and thermal reduction (T-rGO). It has been noticed that the use of different reduction methods impacts the final product properties (sp^2 and sp^3 domains, number of layers, sheets size, number of defects, surface area and surface charges). Furthermore, the electrical conductivity and surface properties of these graphene-based materials (GO, H-rGO, AA-rGO and T-rGO) were also investigated. To the best of our knowledge, there is a paucity of information in the literature that compares the properties of rGO produced by different reduction methods at scale.

2 Experimental

2.1 Materials

Graphite powder (<20 μm , synthetic, Sigma Aldrich), potassium permanganate (KMnO_4 , $\geq 99\%$, Sigma Aldrich), sulphuric acid (H_2SO_4 , 98%, ACE), hydrogen peroxide solution (H_2O_2 30% w/w in H_2O , Sigma Aldrich), hydrochloric acid (HCl, 30% ACE) and ascorbic acid (99%, ACE) were purchased and used as such.

2.2 Synthesis of GO

To balance safety with cost, the ratios for the reactants by weight: 1 graphite: 91.5 H_2SO_4 : 4 KMnO_4 were used. In a typical experiment, 40 g of graphite powder was added to 2.0 L of concentrated H_2SO_4 and stirred for 1 h. This was followed by the slow addition of 160 g of KMnO_4 in few gram quantities (~5.0 g) while stirring. The addition of KMnO_4 into graphite-acid slurry took over 17 min, and the reaction was further allowed to be stirred to dissipate exothermic heat from the reactor. After reaching a maximum temperature of 52 °C, reaction temperature started to decrease and then reaction temperature was set to 50 °C. At 50 °C, the reaction contents are kept in agitation for 6 h to allow for the complete oxidation process. After 6 h, the reaction mixture colour turned brownish, which shows that the reaction is complete. The reactor system was then de-energised and allowed to cool naturally. Upon reaching 30 °C, the mixture was quenched in ice-cooled 4 L of 1% H_2O_2 solution. The reaction solution was allowed to settle naturally to achieve self-precipitation, and then the supernatant was decanted. The slurry was further washed twice with

deionised water using centrifugation to remove salt impurities and unused acid. Furthermore, the remaining insoluble salts were dissolved using an aqueous solution of 5% HCl and washed out with water using centrifugation. The brownish colour precipitation was washed with deionised water several times until the decanted water pH reached ~6. The as-produced graphite oxide was exfoliated into graphene oxide using ultrasonication for 1.5 h. The received aqueous dispersion of GO was again centrifuged at 9500 rpm for 30 min to get precipitation, which was dried in a vacuum oven at 60 °C for 24 h. Finally, 62.2 g of product (GO) was recovered after drying.

2.3 Synthesis of ascorbic acid reduced graphene oxide (AA-rGO)

In the ascorbic acid reduction method, a 5 mg/mL aqueous suspension of GO was prepared in 5L of deionised water using ultrasonication. Next, 100 g of ascorbic acid was added to this solution and stirred for 20 min. The pH of the solution was adjusted to basic medium using 10 g of NaOH to promote colloidal stability via the electrostatic repulsion. The final reaction mixture was stirred and heated at 90 °C for 1 h. After completion, the reduced black product was separated using centrifugation and washed with water to remove excess unreacted products. The precipitated rGO was dried in a vacuum oven at 60 °C; finally, the weight of powdered product AA-rGO was found to be 16.3 g.

2.4 Synthesis of hydrothermally reduced graphene oxide (H-rGO)

In hydrothermal reduction, a GO suspension (5 mg/mL) was prepared in 5 L of deionised water using ultrasonication. This was followed by the addition of 10 g of NaOH to help promote colloidal stability via electrostatic repulsion. The reaction mixture was stirred for 20 min before being transferred to the hydrothermal reactor. The solution was then stirred, while maintained at 185 °C for 3.5 h to allow for the complete reduction process to occur. The black product was separated using centrifugation, washed with copious deionised water. The precipitated rGO was transferred to a vacuum oven at 60 °C for drying; finally, 12.6 g of H-rGO was produced in this process.

2.5 Synthesis of thermally reduced graphene oxide (T-rGO)

In thermal reduction, 25 g of GO was subjected to high temperature in a furnace at 600 °C for 3 min. The high temperature supports the expansion and reduction of GO sheets by eliminating most oxygen-carrying functionalities from basal and edge surfaces. After completing the thermal process, the

sample was naturally cooled down. The sample weight of the thermally reduced graphene (T-rGO) was found to be 10.2 g.

2.6 Characterisation

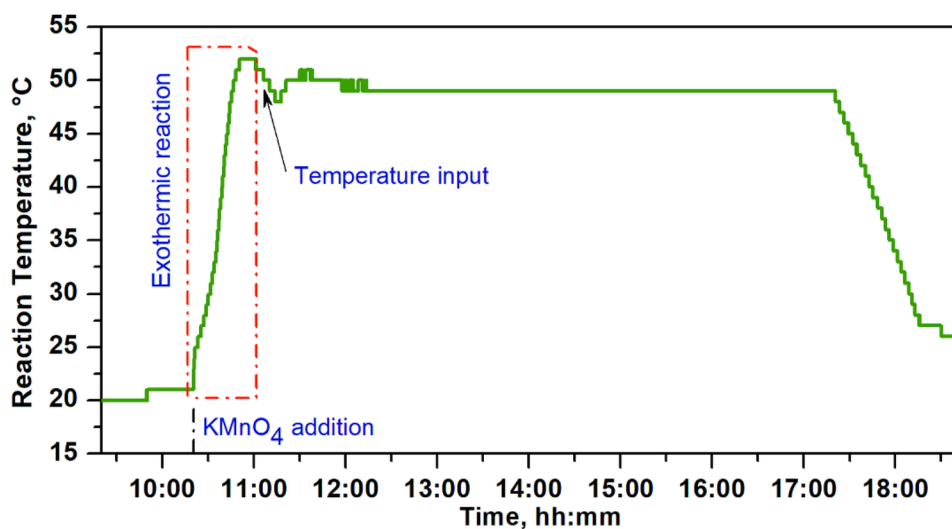
The N_2 adsorption–desorption isotherms were studied on a Micromeritics (ASAP 2020, USA) analyser to calculate specific surface area and porosities of graphene-based materials using the multi-point Brunauer–Emmett–Teller (BET) technique. Fourier transform infrared (FTIR) analysis was done on FTIR spectrometer (PerkinElmer Spectrum100, USA) using FTIR grade KBr as a reference material. The FTIR data were obtained in transmittance mode in the range $4000\text{--}400\text{ cm}^{-1}$ with a spectral resolution of 4 cm^{-1} . The phase and structural features of the graphene materials were determined on a XRD instrument (PAN analytical X-pert PRO, Netherlands). The Cu $K\alpha$ radiation ($\lambda = 0.154\text{ nm}$) (as X-ray source) and operating conditions (current = 40 mA, voltages = 45 kV) with the 2θ range $5^\circ\text{--}90^\circ$ were kept constant for all XRD samples. XPS (Kartos, UK) with a monochromated Al $K\alpha$ X-ray source was employed to calculate the chemical composition and oxidation states of different elements present in the samples. The combustion of graphene samples was performed on a TGA instrument (TA Model TGA Q500). The samples were heated from 30 to $900\text{ }^\circ\text{C}$ at the rate of $10\text{ }^\circ\text{C}/\text{min}$ under N_2 atmosphere. UV–Vis spectroscopy study was performed on LAMBDA 750 UV–Vis–NIR Spectrophotometer (PerkinElmer, USA). To study the D, G and 2D peaks of graphene samples, Raman tests were done on an Alpha 300RAS Plus confocal micro-Raman spectrometer (WiTec Focus Innovations, Germany) that operated at 5.0 mW with a $50\times$ magnifying lens using 532 nm laser excitation. The surface morphologies/structures of the graphene samples were investigated using a scanning electron microscope (SEM) (JEOL JSM-7500F,

Japan). The high-resolution transmission electron microscopy instrument (HRTEM; JEOL, 2100-JEM Japan) operated at a voltage of 200 kV was used to investigate the nano-structural features of graphene materials. The bulk conductivity of samples was measured using an electrical conductivity measurement setup considering the powder pressing approach. The Malvern Zetasizer Nano ZS (Malvern Instruments, Worcestershire, United Kingdom) at $25\text{ }^\circ\text{C}$ was used to calculate zeta potential of samples. The instrument displays the net surface charge (mV) of the suspension by calculating the electrophoretic mobility using the laser Doppler velocity principle. The surface wettability of the samples was characterised by water contact angle measurements using the DSA-100 drop shape analyser (KRÜSS, Germany) at ambient temperature.

3 Result and discussion

High-quality GO was prepared by a scalable chemical process, which employed graphite as a carbon precursor and concentrated H_2SO_4 and $KMnO_4$ as an intercalating agent and an oxidant, respectively. The addition of $KMnO_4$ in the reaction was done in a very controlled way. Adding a very small portion of $KMnO_4$ to the reactor induces the heat flux to quickly increase, which in turn increases the reaction temperature. As soon as $KMnO_4$ dissolves in acid, the temperature starts to decrease (Fig. 1). The temperature increase during this step can be controlled by regulating the addition rate of $KMnO_4$. The slow addition of $KMnO_4$ is recommended. Though it is not yet experimentally confirmed that the intermediate in this process is the reactive Mn_2O_7 , appropriate safety considerations regarding this intermediate were assumed. Thus, the potassium permanganate was added

Fig. 1 Recorded temperature profile for oxidation of graphite to form GO



slowly in milligram quantities to avoid rapid overheating, which could lead to a fire or an explosion in extreme cases. Literature suggests that the reaction of KMnO_4 and H_2SO_4 results in the formation of greenish peroxide manganese heptoxide (Mn_2O_7) intermediate that could cause an explosive reaction if the solution reaction temperature increases above 55°C and solution encounters with organic impurities [20, 36]. In this process, the exothermic reaction temperature for the oxidation process did not increase above 52°C , thus ensuring the process safety and good quality of the product (Fig. 1). On completion of the oxidation reaction, the reaction mixture becomes viscous due to the hydrophilic attraction between different oxygen functional groups ($-\text{OH}$, $-\text{C}=\text{O}$, and $-\text{COOH}$) and H_2O molecules.

Furthermore, for the quenching process, the produced reaction slurry is slowly introduced to water (1% H_2O_2 solution). However, adding the acid mixture to water is a highly exothermic reaction, could cause thermal runaway and hot spots in the absence of sufficient cooling and mixing capacity. Thus, slow addition of the reaction mixture is performed in cooled water with constant stirring. The purpose of the H_2O_2 is to convert any residual KMnO_4 /manganese ions into soluble manganese sulphate in acidic medium and manganese oxides, and ultimately stop the oxidation reaction. Furthermore Fig. 2 shows the schematic diagram of the graphite oxidation process and the three GO reduction processes, respectively.

3.1 Structural and morphological characterisation

X-ray diffraction was used to obtain information about the degree of graphite oxidation, the interlaminar distance, the structure, and the oxidation state of the bulk materials. The interlayer spacing (d -spacing, nm) of GO and rGO samples were calculated using Bragg's law as given by Eq. (1):

$$d = \frac{\lambda}{2\sin\theta}, \quad (1)$$

where λ is the wavelength (nm) of the incident X-rays and θ is the angle (degree) of incidence. The XRD patterns of GO, AA-rGO, H-rGO and T-rGO are shown in Fig. 3a. The XRD pattern of GO exhibits a prominent diffraction peak (002) located at $2\theta = 10.8^\circ$, with a corresponding interlayer distance of 0.78 nm. The expanded d -spacing of GO compared to typical pristine graphite (0.34 nm) is due to the oxidation-induced formation of oxygen-containing functional groups between graphite layers [37].

However, after GO reduction, diffraction patterns of subsequent rGO samples exhibit new, broad, and less intense characteristic peaks at $2\theta = 24.5^\circ$, 25.01° and 24.4° with the corresponding d -spacing of 0.36, 0.35, and 0.36 nm for AA-rGO, H-rGO and T-rGO, respectively. In rGO samples, the broad peaks obtained at $2\theta = \sim 24^\circ\text{--}26^\circ$ corresponds to graphene and are well matched with graphite JCPDS card (no. 75–2078) [38]. Meanwhile, a notable reduction process-induced removal of oxygen functionalities in GO is confirmed by the reduced d -spacing

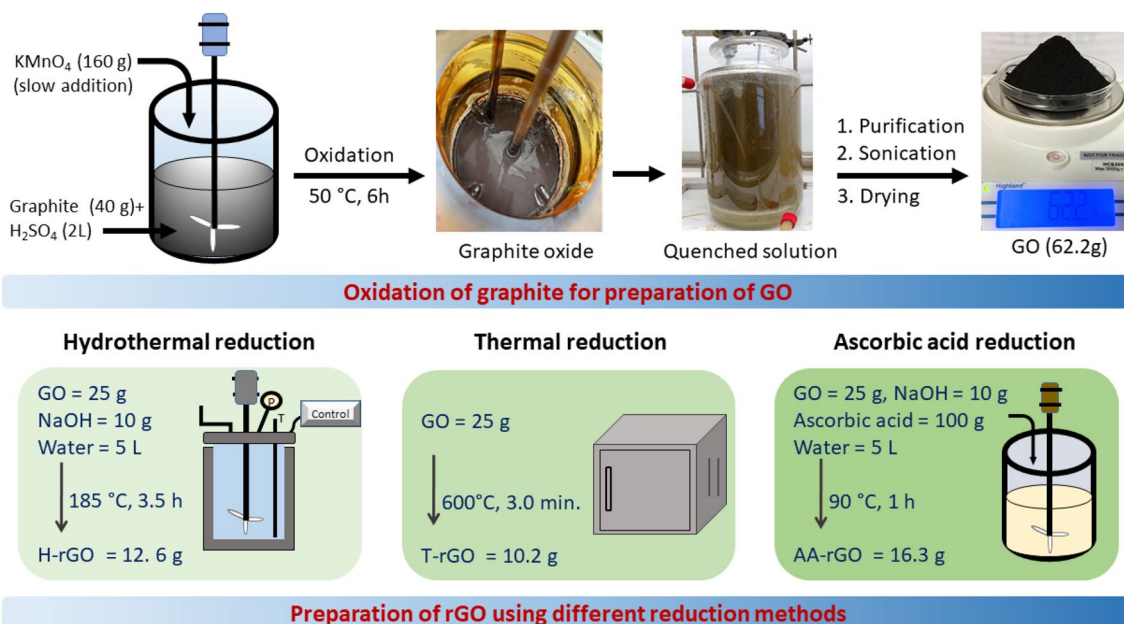


Fig. 2 Schematic shows the critical steps of the scalable synthesis of GO and rGO using different (hydrothermal, thermal, and ascorbic acid) reduction methods

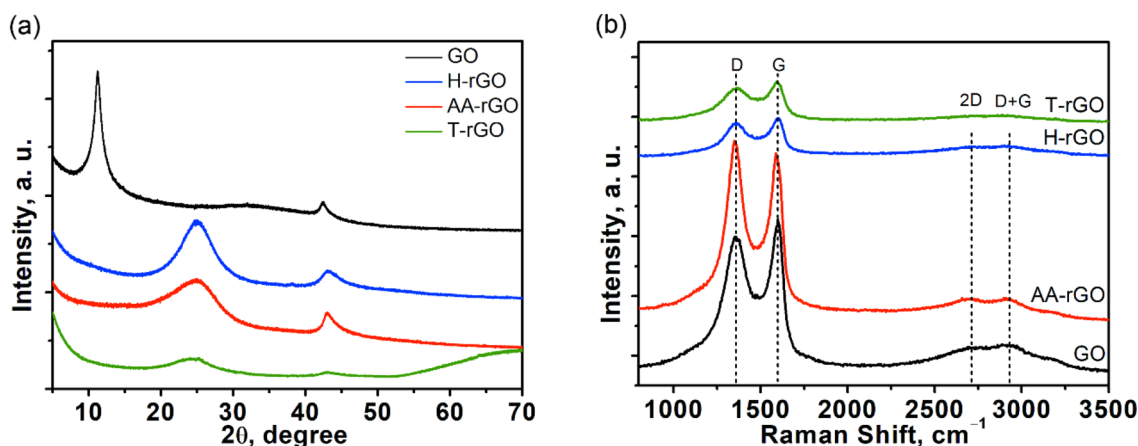


Fig. 3 XRD patterns (a) and Raman spectra (b) of GO, AA-rGO, H-rGO and T-rGO

obtained from the subsequent rGO samples. Furthermore, the structural parameters such as the average stacking crystallite height (D_c), lateral size (D_a) and number (n) of parallel graphene layers per domain were determined from the XRD diffraction patterns using the Scherrer equation (Eq. (2)):

$$D_c \text{ or } D_a = \frac{k\lambda}{\beta \cos \theta}, \quad (2)$$

where λ is the wavelength of the incident X-ray, β is the full peak width of the diffraction peak at half maximum height (FWHM) expressed in radians, and k is the Warren form factor constant related to the crystallite shape. The k values used to calculate D_c and D_a are 0.9 and 1.84, respectively. The calculated structural parameters of the corresponding GO, AA-rGO, H-rGO and T-rGO are summarised in Table 1. Accordingly, the average D_c and D_a of GO was found to decrease upon subsequent reduction from 7.3 and 9.7 nm to 1.2 and 6.6 nm for AA-rGO, 1.5 and 4.7 nm for H-rGO, 1.3 and 3.6 nm for T-rGO. The decrease may be due to the shrinking graphitic domains and the generation of more grain boundaries or lateral defects arising from the expulsion of graphene layers upon reduction of GO [39]. Moreover, the average number of graphene layers (n) per domain were calculated using the both Debye–Scherrer and Bragg’s equations expressed in Eq. (3) as:

$$n = \frac{D_c}{d_{002}}. \quad (3)$$

The average number of layers in GO was found to decrease from 9 to 3 nm, 4, and 4 nm for AA-rGO, H-rGO and T-rGO, respectively, indicating the elimination of oxygen functionalities between individual graphene layers per crystallite upon reduction [39].

Raman spectroscopy was employed to examine the GO structural quality and crystallite size changes with the reduction to subsequent rGO (AA-rGO, H-rGO and T-rGO). The typical Raman spectrum of graphene-based materials exhibits prominent characteristic bands assigned to the first-order effect D (1320–1350 cm^{-1}) and G (1570–1605 cm^{-1}) modes, and the second-order effect 2D (2640–2680 cm^{-1}) mode [40]. The D band corresponds to defects in the graphitic structure, and the G band is the in-plane vibration of the sp^2 C atoms. The 2D band emerges from the second-order double resonant Raman scattering zone boundary [40, 41]. Meanwhile, the shapes, intensities and positions of prominent Raman characteristic bands provide specific information about the structural properties of GO and rGO samples.

Particularly, the relative intensity ratio of the D and G bands (I_D/I_G) is generally used to estimate the disorder degree of graphitic structural defects and is inversely proportional to the effective crystallite size of the sp^2 graphitic domains. Furthermore, the crystallite size (L_a) of a graphitic

Table 1 Structural parameters of GO and rGO samples obtained from XRD and Raman spectroscopy characterisation technique

Sample	XRD				N	Raman		
	d -spacing (nm)	FWHM β ($^\circ$)	D_c (nm)	D_a (nm)		I_D/I_G	I_{2D}/I_G	L_a (nm)
GO	0.78	1.2	7.3	9.7	9	0.90	0.34	4.9
AA-rGO	0.36	6.8	1.2	6.6	3	1.06	0.37	4.1
H-rGO	0.35	5.6	1.5	4.7	4	0.92	0.55	4.7
T-rGO	0.36	6.4	1.3	3.6	4	0.93	0.48	4.7

plane can be determined following the relation proposed by Tuinstra and Koenig [42] in Eq. (4),

$$L_a = 4.4 \frac{I_G}{I_D}, \quad (4)$$

where L_a (nm) is the average crystallite size in the lateral direction of the graphite plate [40]. The Raman spectra of GO and its reduced AA-rGO, H-rGO and T-rGO derivatives are shown in Fig. 3b, and the calculated structural parameters, I_D/I_G and L_a , are summarised in Table 1. As expected, the Raman spectrum of GO exhibits two intense peaks matching Raman characteristic D and G bands at 1359 and 1603 cm^{-1} , respectively, as well as a broad 2D band at 2701 cm^{-1} . The intense D band in GO spectrum indicates graphitic structural defects due to the formation of oxygen functionalities introduced during oxidation. Meanwhile, the relative I_D/I_G of the GO defects were found to be 0.90, while the L_a of the aromatic lamellae was determined as 4.9 nm.

After GO reduction, the spectra of subsequent rGO samples exhibit similar Raman characteristic D, G and 2D peaks but with increased relative I_D/I_G compared to GO. Precisely, the relative I_D/I_G values of 1.07, 0.92 and 0.93

were calculated for AA-rGO, H-rGO and T-rGO samples, respectively. The increasing trend in the relative I_D/I_G values of the rGO indicates the formation of more structural defects due to the elimination of oxygen groups and a decrease in the average L_a of sp^2 domains after GO reduction.

The calculated L_a of 4.1, 4.7 and 4.7 nm for AA-rGO, H-rGO and T-rGO, respectively, show an inverse relationship with relative I_D/I_G values and thus obey Tuinstra-Koenig relation for nano-crystalline substance [40]. The obtained L_a values are slightly different from the D_a values obtained from the XRD data. Moreover, the calculated I_{2D}/I_G values increased from 0.34 for GO to 0.37, 0.55 and 0.48 for AA-rGO, H-rGO and T-rGO, respectively. The higher I_{2D}/I_G values indicate a few graphene layers, suggesting good conformity with the calculated number of layers from the XRD diffraction patterns.

XPS is a crucial technique to predict the quality of graphene-based materials. It was utilised to determine the surface chemistry of as-synthesised GO and rGO samples. Figure 4 exhibits the high-resolution spectra of C 1s of GO, AA-rGO, H-rGO and T-rGO. The C 1s spectrum of GO revealed an overlying doublet peak with a tail towards higher binding energy. It indicates that C is linked to the

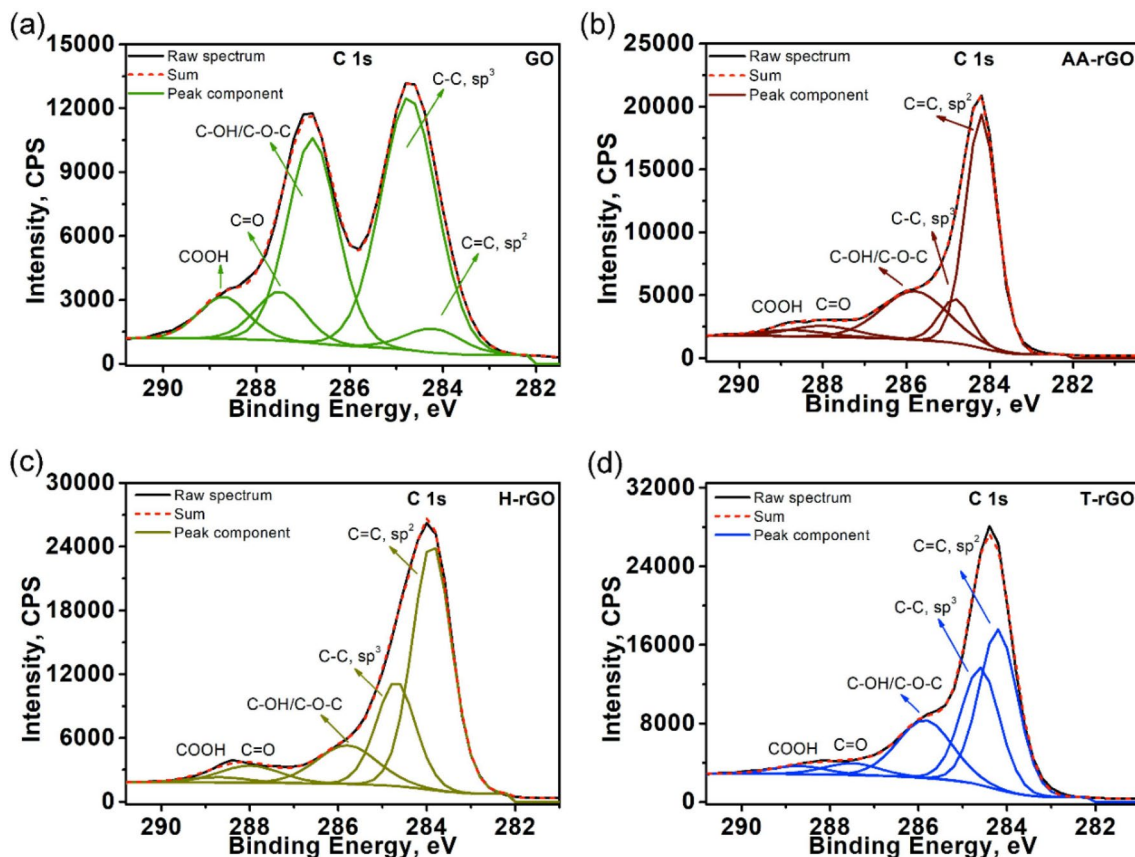
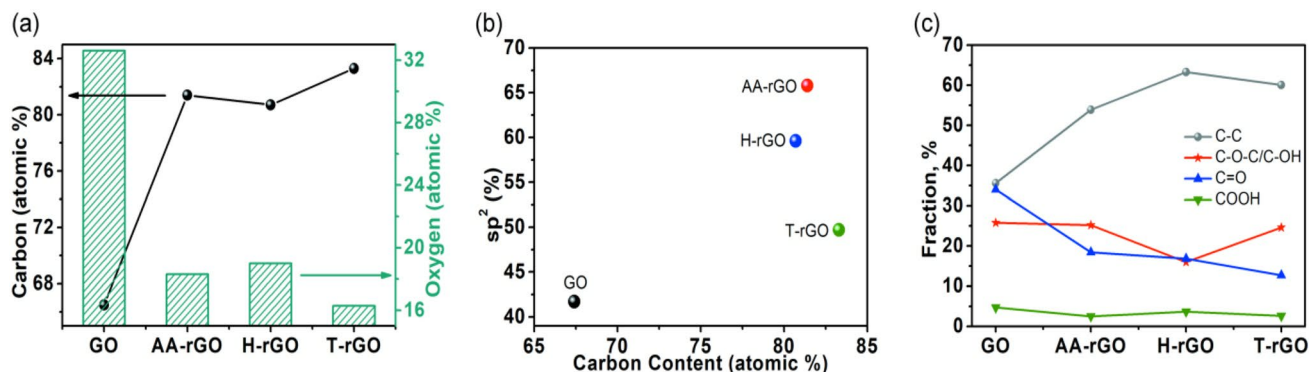


Fig. 4 Deconvoluted core level C 1s XPS spectra of GO (a), AA-rGO (b), H-rGO (c) and T-rGO (d)

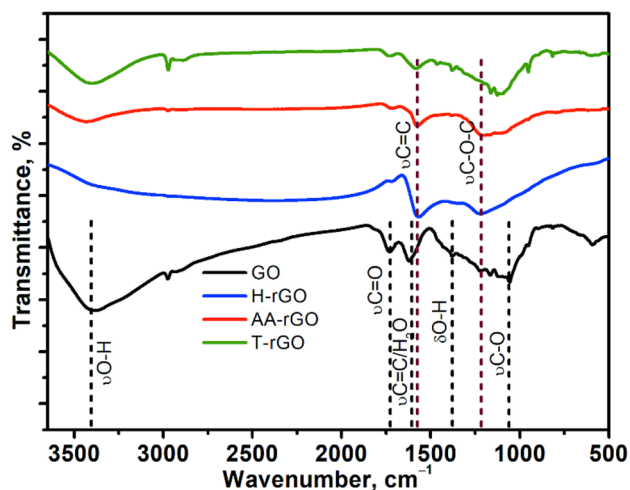
Table 2 Summarise the characteristics of GO, AA-rGO, H-rGO and T-rGO

Samples	C/O (XPS)	Surface area (m ² /g)	Pore volume (cm ³ /g)	Pore size (nm)	Conductivity (S/m)	Zeta potential (eV)	Contact angle (°)
GO	2.04	141.26	0.12	3.3	208.95	−23.13	36
AA-rGO	4.50	29.50	0.05	7.4	608.76	−46.73	114
H-rGO	4.24	383.16	0.21	2.1	194.80	−32.53	112
T-rGO	5.11	368.58	0.71	7.7	389.61	−28.27	122

**Fig. 5** Change in the atomic percentage of carbon and oxygen (a), comparison of sp²% and C content (b), change in fraction% of the C–C and carbon bonded with oxygen functionalities in GO and reduced GO (AA-rGO, H-rGO and T-rGO) (c)

various oxygen functional groups. The C 1s spectrum could be deconvoluted into five peaks at 284.2, 284.7, 286.8, 287.5 and 288.7 eV and was attributed to C=C (sp²), C–C (sp³), C–OH/C–O–C, C=O and –COOH groups of the GO [43]. The reduction of GO to rGO (AA-rGO, H-rGO and T-rGO) demonstrated a significant decrease in oxygen-carrying functionalities. Moreover, the peak maxima of C 1s in the rGO was shifted towards lower binding energy and showed maximum contribution from C=C/C–C/C–H groups [44].

The atomic percentage of C=C (sp²) in different rGO samples follows order as AA-rGO > H-rGO > T-rGO. The atomic ratio of C/O for GO was 2.04, which supports the strong oxidation of graphite (Table 2). The atomic ratio of C/O was increased for rGO samples and followed order as T-rGO (5.11) > AA-rGO (4.50) > H-rGO (4.24) (Fig. 5a). These C/O values were comparable to the previously reported values of GO and rGO [20, 45]. It indicates that oxygen functionalities significantly decreased in the reduced graphene samples. Among different rGO, T-rGO exhibited the lowest value of oxygen, suggesting the high reduction of oxygen-carrying groups. However, the percentage of sp² was higher for AA-rGO than H-rGO and T-rGO (Fig. 5b). The quality of graphene can be defined based on two critical factors- the percentage of sp² and carbon content (C). The results have demonstrated that AA-rGO has the highest quality than H-rGO and T-rGO owing to its highest sp²% and C content of 65.9 and 81.8%,

**Fig. 6** FTIR spectra of GO and AA-rGO, H-rGO and T-rGO

respectively. These values compare favourably to the previously reported values in the literature [46]. The lowest sp²% and high sp³% in T-rGO suggest more defects occurred due to high temperatures. Moreover, Fig. 5c shows the changes in the % of the different oxygen functionalities on the oxidised and reduced graphene materials. These % changes clearly show that the oxidation and reduction processes were successful.

The FT-IR spectrum of GO demonstrates an intense and broad peak at 3388 cm^{-1} , ascribed to the stretching of O–H bonds, indicating the presence of numerous hydroxyl groups on the GO surface (Fig. 6). The lower wavenumber peaks at 1721 , 1621 , 1377 , 1235 – 1150 and 1059 cm^{-1} were assigned to the stretching of carboxy/carbonyl (C=O) groups, the remaining sp^2 -hybridized C after oxidation and trapped water molecules, O–H deformations of the C–OH groups, C–O–C stretching of epoxides and ethers, and C–O (alkoxy) stretching vibrations, respectively. After GO reduction, peaks at 3388 cm^{-1} were decreased in intensity and peak at 1721 cm^{-1} were almost diminished, revealing the decomposition of carboxyl groups. The $-\text{CH}_2$ absorption peaks was noticed at $\sim 2973\text{ cm}^{-1}$ (asymmetric) and $\sim 2899\text{ cm}^{-1}$ (symmetric), ascribed to stretching modes of alkyl groups that formed on reduction of $-\text{COOH}$ groups to $-\text{CH}_3$ segment. The residual intensity of $-\text{OH}$ peak in AA-rGO and T-rGO is related to thermally stable phenolic groups. The shift of 1621 cm^{-1} peaks towards the low wavenumber indicating the removal of trapped H_2O molecules and a slightly increase in peak intensity suggests repairing of sp^2 C in rGO samples. Thus, the appearance of a new peak at 1583 cm^{-1} shows the restoration of sp^2 -carbon networks (C=C) in rGO samples. It is noticed that epoxy groups are thermally stable and removed during hydrothermal reduction, but ether groups are stacked to graphene networks as they are found to be hydrothermally stable [47]. The peak at $\sim 1225\text{ cm}^{-1}$ confirmed the presence of ether groups in rGO samples, which hindered their complete reduction. Moreover, FTIR results showed that phenolic, ether and carboxylic groups were the residual oxygen-carrying functionalities after the reduction of GO using different methods. It was noticed that the ascorbic acid reduction method produced highly reduced graphene as residual oxygen-carrying functionalities having low intensities.

In Fig. 7a, the UV–Vis absorption spectrum of GO reveals a strong peak at 248 nm , which was ascribed to π – π^* transition of remaining aromatic C=C (sp^2) bonds. A shoulder at 301 nm was attributed to n – π^* transition of C=O bonds [37]. The disappearance of this peak in the rGO samples and the appearance of a new peak at $\sim 271\text{ nm}$, which is a typical peak of strongly reduced rGO, noticeably indicate that GO is successfully reduced into rGO [48]. The π – π^* transition band of C=C bonds was shifted to a higher wavelength (~ 271) after conversion of GO to rGO. During the reduction process, π -conjugation or restoration of π -conjugation increased in rGO, which is required less energy for π – π^* transition, resulting in the red shift of the absorption band.

Figure 7b illustrates the TGA curves of GO and different reduced graphene oxides (AA-rGO, H-rGO and T-rGO). The graphene-based materials exhibited distinct three stages of mass loss at $< 100\text{ }^\circ\text{C}$ (I region), 100 – $360\text{ }^\circ\text{C}$ (II region) and 360 – $900\text{ }^\circ\text{C}$ (III region), which related to the water evaporation, thermal decomposition of oxygen functionalities, and carbon combustion, respectively. In GO, the first weight loss (16%) at $100\text{ }^\circ\text{C}$ was attributed to the evaporation of H_2O molecules that are entrapped in the GO. The second weight loss at 100 – $360\text{ }^\circ\text{C}$ was noticed due to the thermal decomposition of thermal liable oxygen functional groups such as hydroxyl, epoxides, carboxylic acids, and β -hydroxyl carboxylic acids. Finally, the high temperature loss was ascribed to carbon combustion and elimination of aromatic carbons ($-\text{C}=\text{C}-$) and complicated functionalities (dioxolane, diketone, lactol and cyclic structures) [49]. In reduced graphene oxide samples, mass loss at $\sim 195\text{ }^\circ\text{C}$ was found to follow the order, T-rGO $<$ AA-rGO $<$ H-rGO, indicating the presence of comparatively more thermal liable functionalities in H-rGO. The extra weight loss in AA-rGO at 225 – $325\text{ }^\circ\text{C}$ was attributed to removing ascorbic acid residues. A high temperature, weight loss behaviour was noticed to be symmetrical in T-rGO, like bimodal in AA-rGO, and heterogeneous in

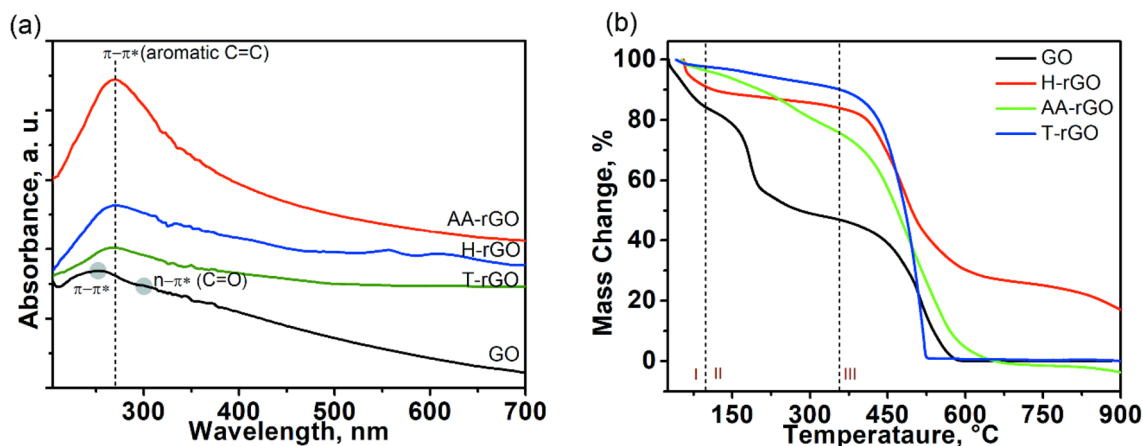


Fig. 7 UV–Vis spectra (a) and TGA graphs (b) of GO, and rGO (AA-rGO, H-rGO and T-rGO)

H-rGO, highlighting the occurrences of different types of oxygen functionalities in rGO. The char yield at 750 °C was observed to follow the order: AA-rGO < T-rGO < H-rGO. It demonstrated that H-rGO carried the highly stable carbon framework among other rGO samples, possibly due to wrinkled-sheet structures. The obtained T_{\max} values (GO = 512.1 °C, AA-rGO = 482.5 °C, H-rGO = 484.2 °C, and T-rGO = 518.4 °C) suggests that formed materials are either GO or rGO; as for GO/rGO, value of T_{\max} must be in range of 475–620 °C (Supplementary information Fig. S1).

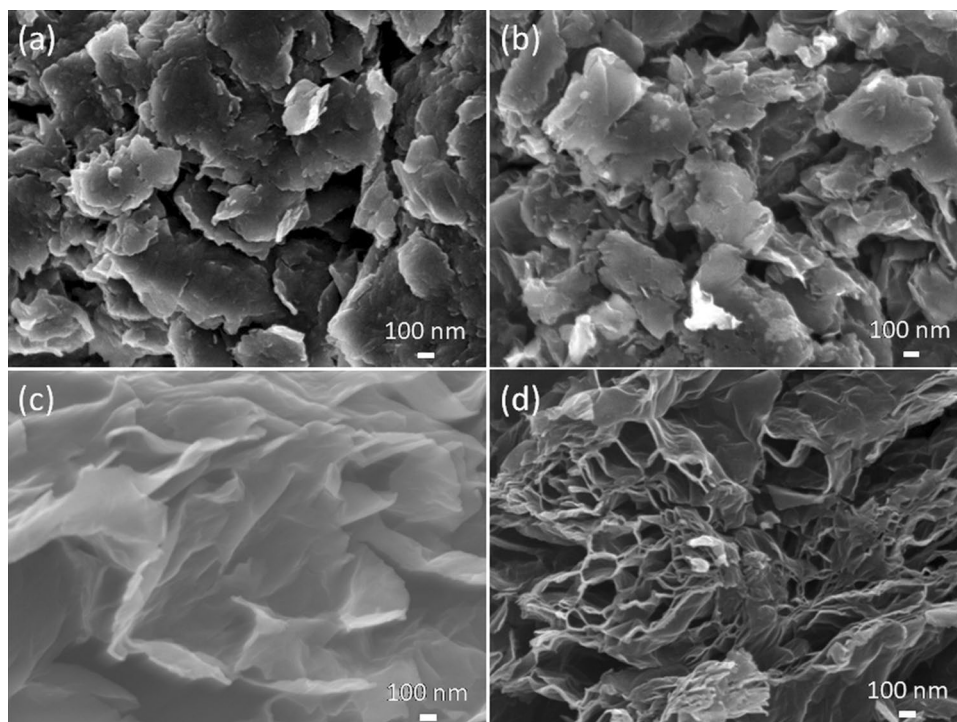
The morphological characteristics of GO and rGO samples are investigated by analysing SEM and TEM images. Figure 8 shows SEM images of GO, AA-rGO, H-rGO and T-rGO to explain the surface morphological changes. The crimped edges carrying re-stacked exfoliated sheets are seen in GO. The stacking pattern of GO has appeared on drying the sample. These sheets consist of multilayers GO platelet, which is also supported by XRD results. After reduction, it was noticed that sheets had shredded and overlapped, leading to curtain-like sheets with zig-zig edges. However, exfoliated sheets and porous structures have been observed in all reduced samples, but T-rGO has shown the highest porous structures with a uniform sheet expansion in the c-axis direction. As noticed in SEM images, the disordered stacking of the rGO sheets is responsible for a broad peak in the XRD pattern.

The partially crumpled and folded features with lateral dimensions in a few hundred nanometres are seen in the GO nanosheets (Fig. 9a, b). The localised intrinsic strain in

sheets is accredited to the presence of sp^3 carbon centres of oxygen functionalities and numerous structural defects in the basal plane of GO sheets, which disturbed smooth 2D structure and produced roughed surfaces. The folded and corrugated morphology is remained in all rGO samples, as it is explicitly seen in TEM images (Fig. 9c–h). As seen in Fig. 9e, f, H-rGO shows highly wrinkled and corrugated morphology because of reduction reaction performed in the hydrothermal autoclave at high-pressure conditions that introduced high localised strain in 2D structure. This could be further supported by the occurrence of ether bonds between sheets and the presence of residual oxygen functional groups along with defects, which is in good agreement with FTIR results. Moreover, T-rGO shows fewer wrinkled features and mostly folds a few layers of graphene sheets. The rGO samples consist of a few layers of graphene sheets in each flake, explaining the integrity of the graphene planes after the chemical/thermal treatments.

The BET surface area is obtained from the nitrogen adsorption–desorption isotherms shown in Fig. 10. The isotherms for GO, AA-rGO, and T-rGO exhibit typical type-IV curves with type H3 hysteresis loops. While the H-rGO exhibits the type-I at low relative pressure and a distinct hysteresis loop at relative pressure from 0.4, indicating the presence of complex pore structures (a combination of microporosity, mesoporosity and some microporosity) [50]. GO display a BET surface area of 141.26 m²/g, which increased to 383.16 m²/g and 368.58 m²/g upon reduction to H-rGO and T-rGO, respectively, as shown in Table 2. The surface

Fig. 8 SEM images of GO (a), AA-rGO (b), H-rGO (c), and T-rGO (d)



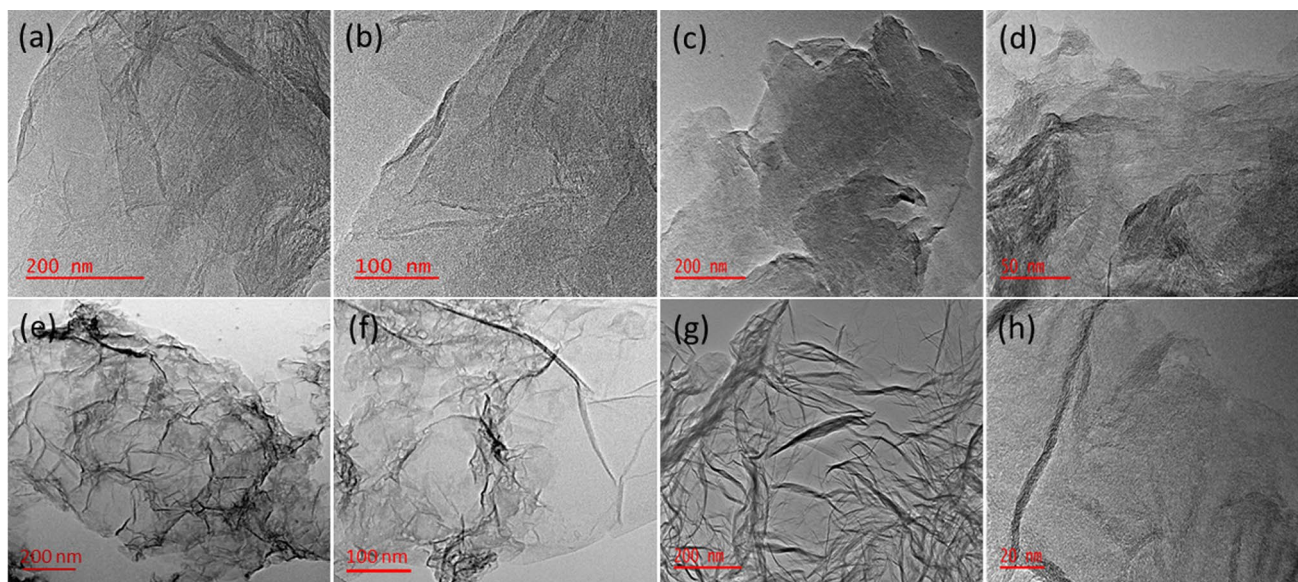


Fig. 9 TEM images of GO (a, b), AA-rGO (c, d), H-rGO (e, f), and T-rGO (g, h)

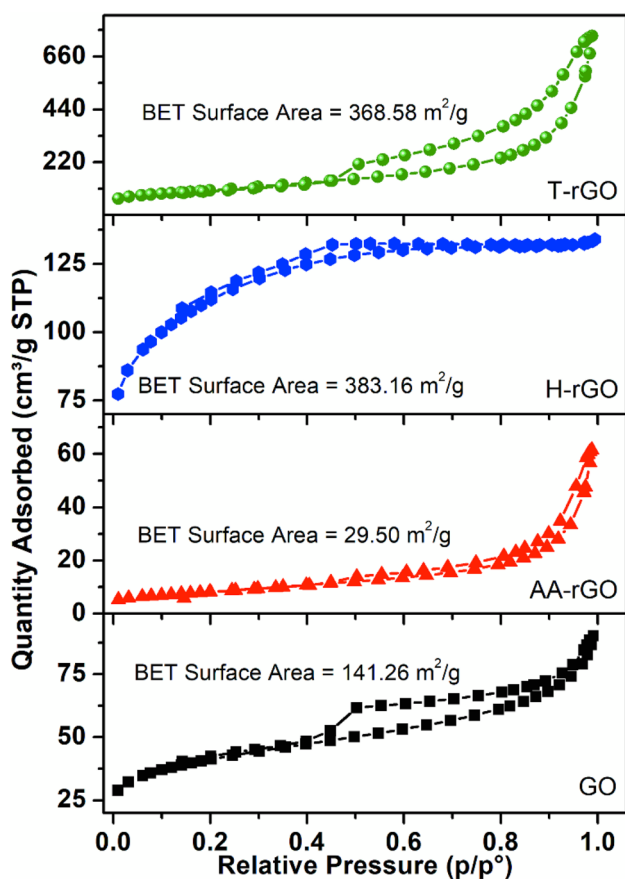


Fig. 10 N_2 gas adsorption–desorption isotherms of GO, AA-rGO, H-rGO and T-rGO samples

area of T-rGO and H-rGO is noticed to be much higher than the reported values of rGO ($254 \text{ m}^2/\text{g}$) [51] ($134.31 \text{ m}^2/\text{g}$) [52]. However, a decrease in the BET surface area of AA-rGO compared to GO is observed, possibly due to the high aggregation of nanosheets with the presence of van der Waals interaction between oxygen functionalities of GO nanosheets and hidden residues of ascorbic acid. Moreover, the surface area of GO and rGO samples was higher than graphite ($7.84 \text{ m}^2/\text{g}$) (Supplementary information Fig. S2). Among all samples, T-rGO shows the highest pore volume ($0.71 \text{ cm}^3/\text{g}$), and average pore diameter (7.7 nm) (Table 1), which is attributed to highly exfoliated defected graphene sheets with residual oxygen functionalities.

Based on spectroscopic results analysis, the plausible mechanism for the chemical changes in the GO during reduction processes is proposed in Fig. 11. The oxidation of graphite introduced various oxygen functionalities such as hydroxyl, carbonyl, epoxide and carboxylic groups onto edges and the basal plane of GO. The hydrothermal reduction of GO can be explained in the following steps: (a) decarboxylation ($-\text{CO}_2$) via eliminating carbon from the GO network, (b) dehydration ($\text{H}^\pm\text{H}_2\text{O}$) to form π bond by eliminating $-\text{OH}$ and adjacent hydrogen, (c) intermolecular dehydration ($\text{H}^\pm\text{H}_2\text{O}$) to form ether bond between two different GO nanosheets, (d) dehydration ($-\text{H}_2\text{O}$) to form cyclic ether, (e) decarboxylation ($-\text{CO}_2$) by consuming the carboxyl group, (f) dehydration ($\text{H}^\pm\text{H}_2\text{O}$) to form epoxide via using two adjacent $-\text{OH}$ group, (g) epoxide to $-\text{OH}$ formation by utilising neighbouring hydrogen [53], and (h) reductive conversion of carbonyl ($-\text{CO}$) group into $-\text{OH}$ group with formation of the π bond. The residual oxygen in H-rGO is mainly related to epoxide, hydroxyl, and carbonyl groups,

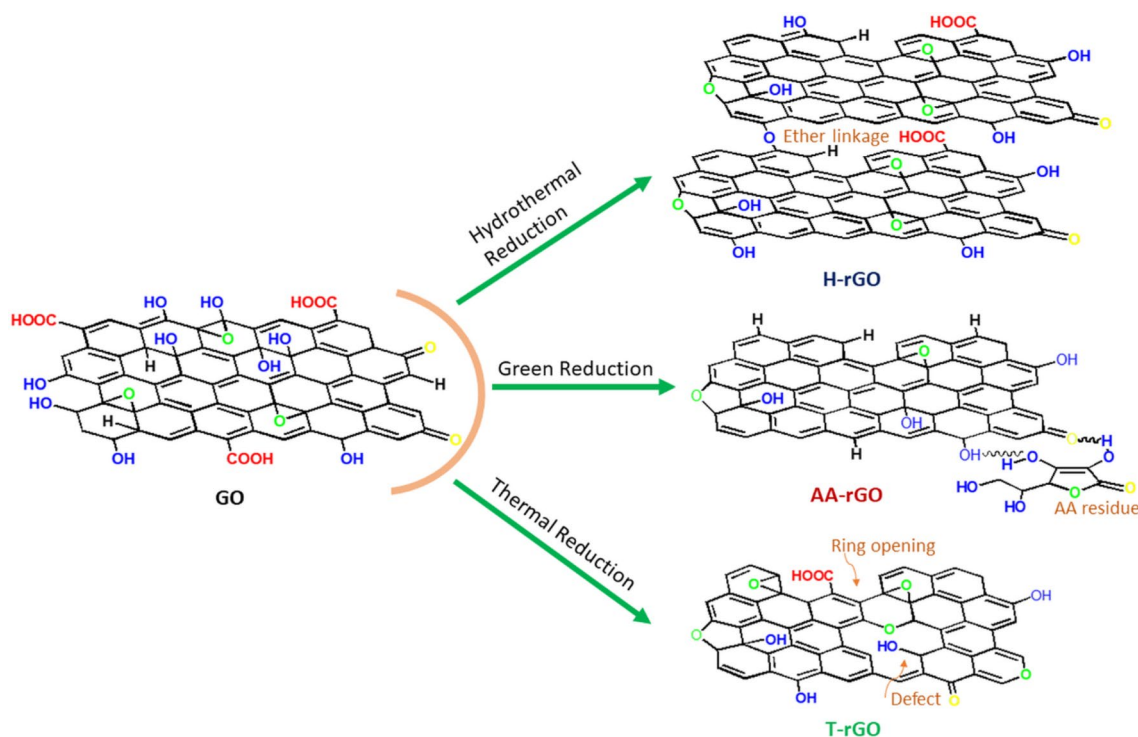


Fig. 11 Schematic diagram of the plausible mechanism for the chemical changes in the GO during thermal, green and hydrothermal reduction

supported by FTIR and XPS. Similar chemical changes were noticed in AA-rGO with the further reduction of epoxide, hydroxyl, and carboxyl groups, which enhances the uninterrupted π network.

Moreover, trapped AA residues could also be seen on green reduction, AA and GO can be linked together by developing intermolecular hydrogen bonds, which TGA well supports. In thermal reduction, low temperature (140–150 °C) results in trapped water molecules evaporation and decomposition of unstable $-\text{COOH}$, $\text{C}-\text{O}-\text{C}$ and $-\text{OH}$ groups. At the same time, high temperature heating

(200–600 °C) produces defects and oxygen doping on T-rGO by forming functional groups such as epoxide and carboxyl at the edges and hole defects sites. Also, high temperature leads to the ring-opening in the carbon network, resulting in an increased number of sp^3 carbons and defects, confirmed by XPS. Moreover, the fluffiness and increased exfoliation of T-rGO are attributed to quick removal of oxygen functionalities and intercalated H_2O , allowing gas access to the pores and the formation of structural defects during elimination of CO_2/CO and $\text{H}_2\text{O}/$

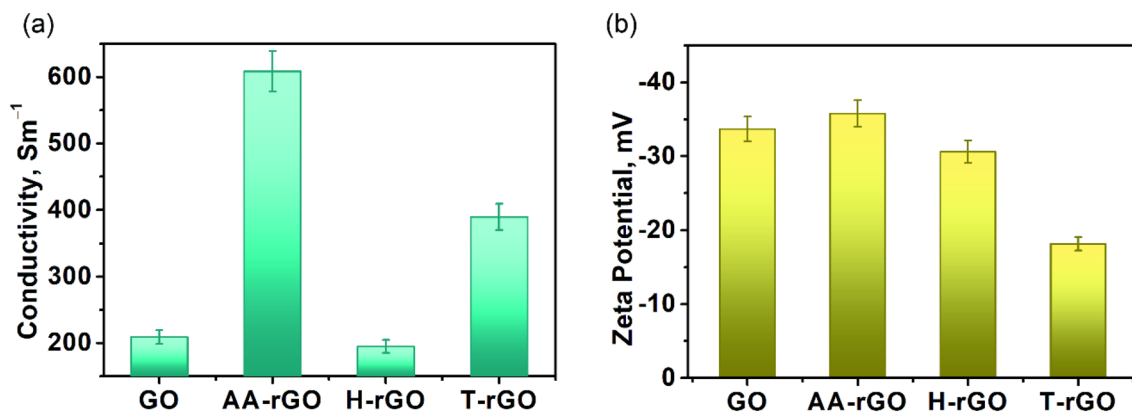
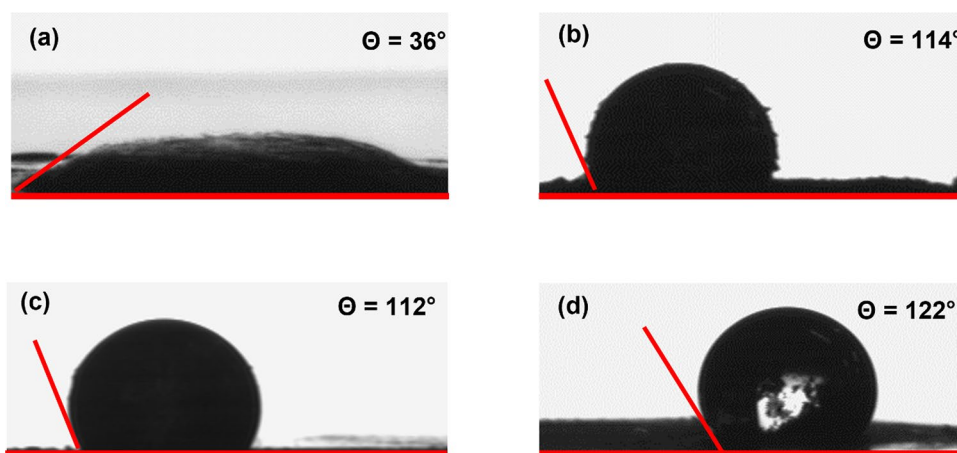


Fig. 12 Electrical conductivity (a) and zeta potentials (b) of GO and reduced GO (AA-rGO, H-rGO and T-rGO)

Fig. 13 Contact angle measurements of GO (a), AA-rGO (b), H-rGO (c) and T-rGO (d)



CO₂ gases. The presence of residual hydroxyl, epoxide, and carboxyl groups was confirmed by FTIR and XPS.

3.2 Surface and electrical conductivity properties

Figure 12a exhibits the bulk electrical conductivity of GO and rGO samples. The as-synthesized GO sheets demonstrated conductivity of 208.50 Sm⁻¹ due to the presence of many graphite domains and a smaller number of defects, which allows easy flow of electrons. The AA-rGO (608.76 Sm⁻¹) showed the highest conductivity among GO and other rGO due to a high percentage of sp² content and fewer defects, allowing easy electron transport throughout the carbon network. The constriction in current flow (low conductivity 194.80 Sm⁻¹) in H-rGO was ascribed to wrinkled and corrugated morphologies of sheets and high content of oxygen functionalities. The obtained values of bulk electrical conductivity of GO and rGO are in good agreement with the reported literature [54, 55].

Zeta potential analysis was used to evaluate the changes in the effective surface charge and stability of GO upon reduction to its reduced AA-rGO, H-rGO and T-rGO derivatives in aqueous solution at pH 6.8. According to the results in Fig. 12b, an average zeta potential of -33.7 mV obtained for GO indicates the presence of a sufficient amount of negative charge density resulting from the oxidation induced -OH and -COOH groups on basal and edge sites of GO. In contrast, to GO, lower average zeta potentials of -30.6 and 18.2 mV can be observed for H-rGO and T-rGO, respectively, whereas a higher zeta potential of -35.8 mV is observed for AA-rGO. The lower zeta potential of H-rGO and T-rGO is due to the decrease in surface charge density by the reduction-induced removal of oxygen functionalities in GO. On the contrary, the higher zeta potential of AA-rGO compared to GO may be due to the increased surface negative charge by the presence of the ascorbic acid functional groups (-OH and -C=O) absorbed on the rGO surface during GO reduction, as they act as a stabilising moiety and thus leading to

more stable dispersion and higher zeta potential values [56]. Moreover, the samples with measured zeta potential values higher than -30 mV indicate excellent stability of the GO, AA-rGO and H-rGO particles dispersion in water, compared to that of T-rGO (-18.2 mV) [57].

The surface wetting properties were determined from the static water contact angle (WCA) measurements of water droplets on the surface of the GO, AA-rGO, H-rGO and T-rGO samples, as shown in Fig. 13. The GO sample in Fig. 13(a) display complete wettability with the measured average WCA of 36°, suggesting excellent hydrophilic properties of GO. Such excellent hydrophilic properties result from oxidation-induced oxygen functionalities in the GO structure. After reduction, the WCA of GO increased to 114°, 112° and 122° for the reduced AA-rGO, H-rGO and T-rGO, respectively. Moreover, the observed hydrophobicity in the subsequent rGO samples is owing to the reduction-induced elimination of main hydrophilic functional carboxyl and hydroxy groups in GO.

Comparison of different reducing agents for the conversion of GO to rGO has demonstrated in Table 3. It was noticed that as-optimized reduction methods produced good quality rGO compared to other methods.

4 Conclusion

The processes of producing GO and rGO were demonstrated in batch systems. The oxidation/reduction processes described here produced GO and rGO with characteristics that compare favourably with the reported literature and are scalable. Following the oxidation step, the rGO materials produced, based on hydrothermal, thermal, and ascorbic acid reduction (green) processes, have different properties that make them suited for various applications. These reduction methods were further optimised to produce a large quantity of rGO per batch (> 10 g). Raman spectroscopy and XRD patterns of the rGO materials shows

Table 3 Comparison of different reducing agents for the conversion of GO to rGO

Reducing Agents	T (°C)	Time	C/O ratio	Conductivity (Sm ⁻¹)	References
Ethanol	100	5 days	6	1.8 × 10 ⁻⁴	[58]
Urea/NH ₃	95	30 h	4.5	43	[59]
Na-citrate	95	18 h	4.7	30.6	[60]
L-Ascorbic acid/L-tryptophan/NaOH	80	24 h	–	14	[61]
Green tea	90	2.5 h	–	53	[62]
L-Cysteine	RT	72 h	–	1.2 × 10 ⁻¹	[63]
Thermal annealing in ultra-high vacuum	900	5 min	14.1	–	[64]
Se powder (solid state reaction)	360	5 min	35	–	[65]
Hydrazine	90	2 h	7	164	[66]
Ascorbic acid/NaOH	90	1 h	4.50	608.76	Present study
Hyrtothermal	185	3.5 h	4.24	194.80	Present study
Thermal reduction	600	3 min	5.11	389.61	Present study

all the typical characteristics of few-layer graphene (FLG). The results have demonstrated that AA-rGO has the highest quality than H-rGO and T-rGO owing to its highest sp² and C content of 65.9 and 81.8%, respectively. Furthermore, AA-rGO revealed the highest electrical conductivity due to an uninterrupted sp² carbon network and a more uniform flat surface with fewer defects. The relatively low electrical conductivities of the rGO samples (H-rGO and T-rGO) confirm that removing oxygen functionalities from GO left a high number of gaps/defects within the lattice and the corrugated structures. The increased surface area of rGO further supports the fluffy and highly exfoliated characteristics. Additionally, WCA shows GO drops its hydrophilicity after the reduction, producing rGO samples with good hydrophobicity, which further reaffirms the removal of oxygen moieties during reduction. Moreover, zeta potential studies of GO (–33.7 mV), AA-rGO (–35.8 mV), and H-rGO (–30.6 mV) particles dispersed in water demonstrated excellent stability, compared to that of T-rGO (–18.2 mV). Among reduction methods, the ascorbic acid reduction is the best approach to obtain high-quality graphene. As such, rGO materials might not be helpful in high-end electronics but are suitable for catalysis, energy storage, environmental remediation, biomedical applications, and low-value, high-volume applications such as composites.

Supplementary Information The online version contains supplementary material available at <https://doi.org/10.1007/s42823-022-00335-9>.

Acknowledgements The authors would like to thank the Council for Scientific and Industrial Research, South Africa (2D PG Grant no. C1BCH57) and the University of Johannesburg, South Africa, for financial support.

Declarations

Conflict of interest The authors declare that they have no conflict of interest.

References

- Brownson DA, Kampouris DK, Banks CE (2011) An overview of graphene in energy production and storage applications. *J Power Sources* 196:4873–4885
- Tiwari SK, Thakur AK, Adhikari AD, Zhu Y, Wang N (2020) Current research of graphene-based nanocomposites and their application for supercapacitors. *Nanomaterials* 10:2046
- Torresi F, Hasan T, Wu W, Sun Z, Lombardo A, Kulmala TS, Hsieh G-W, Jung S, Bonaccorso F, Paul PJ, Chu D, Ferrari AC (2012) Inkjet-printed graphene electronics. *ACS Nano* 6:2992–3006
- Qiu B, Xing M, Zhang J (2018) Recent advances in three-dimensional graphene based materials for catalysis applications. *Chem Soc Rev* 47:2165–2216
- Zhao S, Zhao Z, Yang Z, Ke L, Kitipornchai S, Yang J (2020) Functionally graded graphene reinforced composite structures: A review. *Eng Struct* 210:110339
- Gusain R, Kumar N, Ray SS (2020) Recent advances in carbon nanomaterial-based adsorbents for water purification. *Coord Chem Rev* 405:213111
- Kumar N, Kumar S, Gusain R, Manyala N, Eslava S, Ray SS (2020) Polypyrrole-promoted rGO–MoS₂ nanocomposites for enhanced photocatalytic conversion of CO₂ and H₂O to CO, CH₄, and H₂ products. *ACS Appl Energy Mater* 3:9897–9909
- Maswanganyi S, Gusain R, Kumar N, Fosso-Kankeu E, Waanders FB, Ray SS (2021) Bismuth molybdate nanoplates supported on reduced graphene oxide: an effective nanocomposite for the removal of naphthalene via adsorption-photodegradation. *ACS Omega* 6:16783–16794
- Song S, Shen H, Wang Y, Chu X, Xie J, Zhou N, Shen J (2020) Biomedical application of graphene: from drug delivery, tumor therapy, to theranostics. *Colloids Surf B Biointerfaces* 185:110596
- Wu Z-S, Zhou G, Yin L-C, Ren W, Li F, Cheng H-M (2012) Graphene/metal oxide composite electrode materials for energy storage. *Nano Energy* 1:107–131
- Cai X, Lai L, Shen Z, Lin J (2017) Graphene and graphene-based composites as Li-ion battery electrode materials and their application in full cells. *J Mater Chem A* 5:15423–15446
- Yao G, Yang S, He J, Jiang S, Sun C, Song S (2021) In situ growing graphene on g-C₃N₄ with barrier-free interface and polarization electric field for strongly boosting solar energy conversion into H₂ energy. *Appl Catal B Environ* 287:119986

13. Garcia-Segura S, Brillas E (2017) Applied photoelectrocatalysis on the degradation of organic pollutants in wastewaters. *J Photochem Photobiol C* 31:1–35
14. Ma T, Fan Q, Li X, Qiu J, Wu T, Sun Z (2019) Graphene-based materials for electrochemical CO₂ reduction. *J CO₂ Util* 30:168–182
15. Geioushy RA, Khaled MM, Hakeem AS, Alhooshani K, Basheer C (2017) High efficiency graphene/Cu₂O electrode for the electrochemical reduction of carbon dioxide to ethanol. *J Electroanal Chem* 785:138–143
16. Choi S, Kim C, Suh JM, Jang HW (2019) Reduced graphene oxide-based materials for electrochemical energy conversion reactions. *Carbon Energy* 1:85–108
17. Bøggild P (2018) The war on fake graphene. *Nature* 562:502–503
18. Kauling AP, Seefeldt AT, Pisoni DP, Pradeep RC, Bentini R, Oliveira RVB, Novoselov KS, Castro Neto AH (2018) The worldwide graphene flake production. *Adv Mater* 30:1803784
19. Kovtun A, Treossi E, Mirota N, Scidà A, Liscio A, Christian M, Valorosi F, Boschi A, Young RJ, Galiotis C (2019) Benchmarking of graphene-based materials: real commercial products versus ideal graphene. *2D Mater* 6:025006
20. Kumar N, Salehiyan R, Chauke V, Joseph Botlhoko O, Setshedi K, Scriba M, Masukume M, Sinha Ray S (2021) Top-down synthesis of graphene: a comprehensive review. *FlatChem* 27:100224
21. Muñoz R, Gómez-Aleixandre C (2013) Review of CVD synthesis of graphene. *Chem Vap Depos* 19:297–322
22. Polsen ES, McNerny DQ, Viswanath B, Pattinson SW, John Hart A (2015) High-speed roll-to-roll manufacturing of graphene using a concentric tube CVD reactor. *Sci Rep* 5:10257
23. Ye R, Tour JM (2019) Graphene at fifteen. *ACS Nano* 13:10872–10878
24. Tiwari SK, Sahoo S, Wang N, Huczko A (2020) Graphene research and their outputs: status and prospect. *J Sci Adv Mater Devices* 5:10–29
25. Novoselov KS, Geim AK, Morozov SV, Jiang D, Zhang Y, Dubonos SV, Grigorieva IV, Firsov AA (2004) Electric field effect in atomically thin carbon films. *Science* 306:666–669
26. McAllister MJ, Li J-L, Adamson DH, Schniepp HC, Abdala AA, Liu J, Herrera-Alonso M, Milius DL, Car R, Prud'homme RK, Aksay IA (2007) Single sheet functionalized graphene by oxidation and thermal expansion of graphite. *Chem Mater* 19:4396–4404
27. Marciano DC, Kosynkin DV, Berlin JM, Sinitskii A, Sun Z, Slesarev A, Alemany LB, Lu W, Tour JM (2010) Improved synthesis of graphene oxide. *ACS Nano* 4:4806–4814
28. Brisebois PP, Siaj M (2020) Harvesting graphene oxide—years 1859 to 2019: a review of its structure, synthesis, properties and exfoliation. *J Mater Chem C* 8:1517–1547
29. Brodie BC (1859) On the Atomic Weight of Graphite. *Phil Trans R Soc Lond* 149:249–259
30. Staudenmaier L (1898) Verfahren zur Darstellung der Graphitsäure. *Ber Dtsch Chem Ges* 31:1481–1487
31. Hummers WS, Offeman RE (1958) Preparation of graphitic oxide. *J Am Chem Soc* 80:1339–1339
32. Peng L, Xu Z, Liu Z, Wei Y, Sun H, Li Z, Zhao X, Gao C (2015) An iron-based green approach to 1-h production of single-layer graphene oxide. *Nat Commun* 6:5716
33. Chen J, Yao B, Li C, Shi G (2013) An improved Hummers method for eco-friendly synthesis of graphene oxide. *Carbon* 64:225–229
34. Abdolhosseinzadeh S, Asgharzadeh H, Seop Kim H (2015) Fast and fully-scalable synthesis of reduced graphene oxide. *Sci Rep* 5:10160
35. Lavin-Lopez MDP, Romero A, Garrido J, Sanchez-Silva L, Valverde JL (2016) Influence of different improved hummers method modifications on the characteristics of graphite oxide in order to make a more easily scalable method. *Ind Eng Chem Res* 55:12836–12847
36. Lakhe P, Kulhanek DL, Zhao X, Papadaki MI, Majumder M, Green MJ (2020) Graphene oxide synthesis: reaction calorimetry and safety. *Ind Eng Chem Res* 59:9004–9014
37. Verma S, Mungse HP, Kumar N, Choudhary S, Jain SL, Sain B, Khatri OP (2011) Graphene oxide: an efficient and reusable carbocatalyst for aza-Michael addition of amines to activated alkenes. *Chem Commun* 47:12673–12675
38. Shalaby A, Nihtianova D, Markov P, Staneva A, Iordanova R, Dimitriev Y (2015) Structural analysis of reduced graphene oxide by transmission electron microscopy. *Bul Chem Commun* 47:291–295
39. Sharma R, Chadha N, Saini P (2017) Determination of defect density, crystallite size and number of graphene layers in graphene analogues using X-ray diffraction and Raman spectroscopy. *Indian J Pure Appl Phys* 55:625–629
40. Lesiak B, Trykowski G, Tóth J, Biniak S, Kövér L, Rangam N, Stobinski L, Malolepszy A (2021) Chemical and structural properties of reduced graphene oxide—dependence on the reducing agent. *J Mater Sci* 56:3738–3754
41. Ferrari AC (2007) Raman spectroscopy of graphene and graphite: disorder, electron-phonon coupling, doping and nonadiabatic effects. *Solid State Commun* 143:47–57
42. Tuinstra F, Koenig JL (1970) Raman spectrum of graphite. *J Chem Phys* 53:1126–1130
43. Kumar N, Fosso-Kankeu E, Ray SS (2019) Achieving controllable MoS₂ nanostructures with increased interlayer spacing for efficient removal of Pb(II) from aquatic systems. *ACS Appl Mater Interfaces* 11:19141–19155
44. Joshi N, da Silva LF, Jadhav HS, Shimizu FM, Suman PH, M'Peko J-C, Orlandi MO, Seo JG, Mastelaro VR, Oliveira ON (2018) Yolk-shelled ZnCo₂O₄ microspheres: surface properties and gas sensing application. *Sens Actuators B Chem* 257:906–915
45. Stankovich S, Dikin DA, Piner RD, Kohlhaas KA, Kleinhammes A, Jia Y, Wu Y, Nguyen ST, Ruoff RS (2007) Synthesis of graphene-based nanosheets via chemical reduction of exfoliated graphite oxide. *Carbon* 45:1558–1565
46. Islam A, Mukherjee B, Pandey KK, Keshri AK (2021) Ultrafast, chemical-free, mass production of high quality exfoliated graphene. *ACS Nano* 15:1775–1784
47. Bagri A, Mattevi C, Acik M, Chabal YJ, Chhowalla M, Shenoy VB (2010) Structural evolution during the reduction of chemically derived graphene oxide. *Nat Chem* 2:581–587
48. Khan M, Al-Marri AH, Khan M, Mohri N, Adil SF, Al-Warthan A, Siddiqui MRH, Alkhatlan HZ, Berger R, Tremel W, Tahir MN (2014) *Pulicaria glutinosa* plant extract: a green and eco-friendly reducing agent for the preparation of highly reduced graphene oxide. *RSC Adv* 4:24119–24125
49. Farivar F, Yap PL, Hassan K, Tung TT, Tran DNH, Pollard AJ, Losic D (2021) Unlocking thermogravimetric analysis (TGA) in the fight against “Fake graphene” materials. *Carbon* 179:505–513
50. Srinivas G, Zhu Y, Piner R, Skipper N, Ellerby M, Ruoff R (2010) Synthesis of graphene-like nanosheets and their hydrogen adsorption capacity. *Carbon* 48:630–635
51. Li H, Zou L, Pan L, Sun Z (2010) Using graphene nano-flakes as electrodes to remove ferric ions by capacitive deionization. *Sep Purif Technol* 75:8–14
52. Deng F, Pei X, Luo Y, Luo X, Dionysiou DD, Wu S, Luo S (2016) Fabrication of hierarchically porous reduced graphene oxide/SnIn₄S₈ composites by a low-temperature co-precipitation strategy and their excellent visible-light photocatalytic mineralization performance. *Catalysts* 6:113
53. Kim S, Zhou S, Hu Y, Acik M, Chabal YJ, Berger C, de Heer W, Bongiorno A, Riedo E (2012) Room-temperature metastability of multilayer graphene oxide films. *Nat Mater* 11:544–549

54. Marinho B, Ghislandi M, Tkalya E, Koning CE, de With G (2012) Electrical conductivity of compacts of graphene, multi-wall carbon nanotubes, carbon black, and graphite powder. *Powder Technol* 221:351–358
55. Xu C, Shi X, Ji A, Shi L, Zhou C, Cui Y (2015) Fabrication and characteristics of reduced graphene oxide produced with different green reductants. *PLoS ONE* 10:e0144842
56. Ghosh TK, Sadhukhan S, Rana D, Bhattacharyya A, Chattopadhyay D, Chakraborty M (2019) Green approaches to synthesize reduced graphene oxide and assessment of its electrical properties. *Nano-Struct Nano-Objects* 19:100362
57. Konkena B, Vasudevan S (2012) Understanding aqueous dispersibility of graphene oxide and reduced graphene oxide through pKa measurements. *J Phys Chem Lett* 3:867–872
58. Dreyer DR, Murali S, Zhu Y, Ruoff RS, Bielawski CW (2011) Reduction of graphite oxide using alcohols. *J Mater Chem* 21:3443–3447
59. Lei Z, Lu L, Zhao X (2012) The electrocapacitive properties of graphene oxide reduced by urea. *Energy Environ Sci* 5:6391–6399
60. Wan W, Zhao Z, Hu H, Gogotsi Y, Qiu J (2013) Highly controllable and green reduction of graphene oxide to flexible graphene film with high strength. *Mater Res Bull* 48:4797–4803
61. Gao J, Liu F, Liu Y, Ma N, Wang Z, Zhang X (2010) Environment-friendly method to produce graphene that employs vitamin C and amino acid. *Chem Mater* 22:2213–2218
62. Wang Y, Shi Z, Yin J (2011) Facile synthesis of soluble graphene via a green reduction of graphene oxide in tea solution and its biocomposites. *ACS Appl Mater Interfaces* 3:1127–1133
63. Chen D, Li L, Guo L (2011) An environment-friendly preparation of reduced graphene oxide nanosheets via amino acid. *Nanotechnology* 22:325601
64. Pei S, Cheng H-M (2012) The reduction of graphene oxide. *Carbon* 50:3210–3228
65. Tiwari SK, Huczko A, Oraon R, De Adhikari A, Nayak GC (2016) A time efficient reduction strategy for bulk production of reduced graphene oxide using selenium powder as a reducing agent. *J Mater Sci* 51:6156–6165
66. Shang YU, Zhang D, Liu Y, Guo C (2015) Preliminary comparison of different reduction methods of graphene oxide. *Bull Mater Sci* 38:7–12

Publisher's Note Springer Nature remains neutral with regard to jurisdictional claims in published maps and institutional affiliations.

Authors and Affiliations

Neeraj Kumar^{1,2}  · Katlego Setshedi¹ · Mike Masukume¹ · Suprakas Sinha Ray^{1,2} 

✉ Neeraj Kumar
ynk.neeraj@gmail.com

✉ Suprakas Sinha Ray
rsuprakas@csir.co.za

for Scientific and Industrial Research, Pretoria 0001, South Africa

² Department of Chemical Sciences, University of Johannesburg, Doornfontein 2028, South Africa

¹ Centre for Nanostructures and Advanced Materials, DSI-CSIR Nanotechnology Innovation Centre, Council